Electronic Supplementary Information (ESI) available

In situ synthesis of 3D flower-like NiMnFe mixed oxides as monolith catalysts for selective catalytic reduction of NO with NH_3

Hongrui Li,[a] Dengsong Zhang, *[a,b] Phornphimon Maitarad,[a] Liyi Shi,[a,b] Ruihua Gao,[a] Jianping Zhang[b] and Weiguo Cao[b]

[a] *Research Center of Nano Science and Technology, Shanghai University, Shanghai 200444, P. R. China. Fax: 86 -21-66134852; E-mail: dszhang@shu.edu.cn*

[b] *Department of Chemistry, Shanghai University, Shanghai 200444, P. R. China.*

Part I. Experimental details

Materials Preparation

All chemicals were of analytical grade, purchased from Shanghai Chemical Reagents Company and used without further purification. A commercial iron wire mesh (Q235, 60 mesh screen) was used as substrates. It has a hole opening size of approximately 0.9 mm and a wire diameter of 0.27 mm. The wire mesh was cut into pieces (8 cm×1 cm) and pretreated with 0.1 M HCl aqueous solution upon ultrasonic vibration for 5 min to remove dirt and grease, and then it was rolled into a cylindrical form (IWM-C).

In a typical synthesis, 11 mmol of $Ni(NO_3)_2 \cdot 6H_2O$, 11 mmol of $Mn(NO_3)_2 \cdot 6H_2O$, 11 mmol of NH_4Cl, and 0.06 mmol of sodium citrate were dissolved in 40 mL of water under stirring. An ammonia solution of

6% was added dropwise into the obtained solution with vigorous stirring until the pH value is 6-7. The homogeneous solution prepared above was transferred into a Teflon-lined stainless steel autoclave. After the cleaned IWM-C was immersed in the homogeneous solution, the autoclave was heated and maintained at 150 ^{o}C for 12 h and then allowed to cool down to room temperature naturally. The substrate was washed several times with distilled water, dried at 100 ^{o}C for 2 h, and finally calcined in air at 500 ^{o}C for 5 h. The NiMnFe mixed oxide powders were obtained by replacing the iron substrate with $Fe(NO_3)_3$ and using a similar process to that described above.

Characterization

The morphology and elemental information of as-synthesized samples was monitored by using a scanning electron microscope (SEM, JEOL JSM-6700F) with an energy dispersive X-ray spectrometry (EDX). The samples were deposited on a sample holder with a piece of adhesive carbon tape and were then sputtered with a thin film of gold. Powder X-ray diffraction (XRD) was performed with a Rigaku D/MAX-RB X-ray diffractometer by using Cu Kα (40 kV, 40 mA) radiation and a secondary beam graphite monochromator. The X-ray photoelectron spectroscopy (XPS) were recorded on a Perkin–Elmer PHI 5000C ESCA system equipped with a dual X-ray source, using the Mg Kα (1253.6 eV) anode and a hemispherical energy analyzer. The background pressure during data acquisition was kept below 10^{-6} Pa. All binding energies were calibrated using contaminant carbon (C1s = 284.6 eV) as a reference. Inductively Coupled Plasma-Atomic Emission Spectroscopy (ICP-AES) was performed on a Plasma-400. The temperature-programmed reduction by hydrogen (H_2-TPR) was obtained on a Tianjin XQ TP5080 auto-adsorption apparatus. The calcined catalyst was outgassed at 300 °C under N_2 flow for 2 h. After cooling to room temperature under N_2 flow, the flowing gas was switched to a mixture of 5% H_2 - 95% N_2, and the sample was heated to 900 °C at a ramping rate of 10 °C/min. The H_2 consumption was monitored by a TCD.

Catalytic tests

The SCR catalytic experiments were carried out at atmospheric pressure in a fixed-bed stainless steel flow reactor (i.d. 1 cm). The temperature of the reactor was monitored and controlled by thermocouples that were inserted into the center of the catalyst bed. The reactant gases were fed to the reactor by an electronic mass flow controller. The typical reactant gas composition was as follows: 500 ppm NO, 500 ppm NH_3, 3 vol% O_2 and N_2 as balance. The NO-SCR experiments were performed over catalysts from 100 to 470 °C and the gas hourly space velocity was 20000 h^{-1}. The inlet and outlet concentration of NO from reactor was analyzed by a NO-NOx analyzer (KM9106). The concentrations of N_2O and NH_3 were measured by a Transmitter IR N_2O analyzer and IQ350 ammonia analyzer.

All of the stream lines were kept approximately 110 °C to prevent condensation of water and dissolution of NH_3 in water.

Part II. Supplementary XRD patterns, SEM images, elemental data and catalytic experimental results

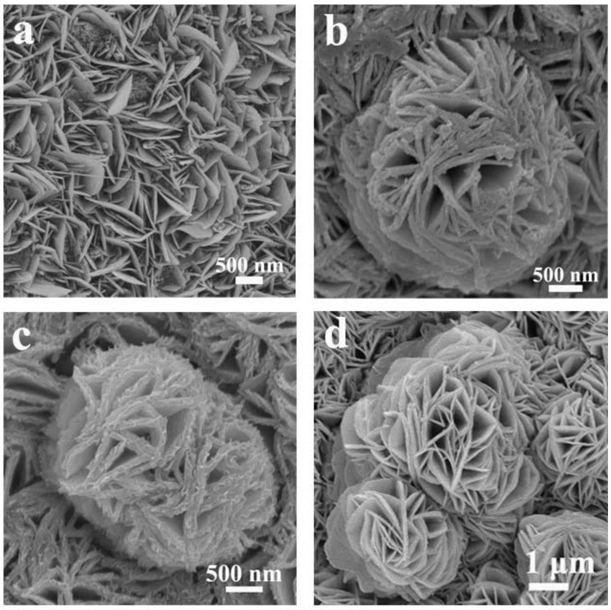

Fig. S1 SEM images of NiMnFe-IWM-C prepared with different reaction time: (a) 2 h, (b) 4 h, (c) 10 h and (d) 12 h.

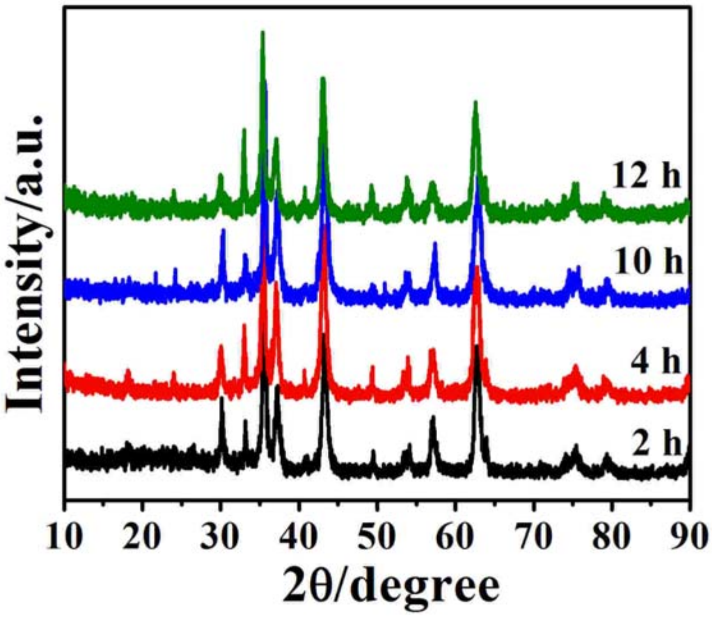

Fig. S2 XRD patterns of NiMnFe-IWM-C prepared with different reaction time. The powders are scraped from the iron wire meshes.

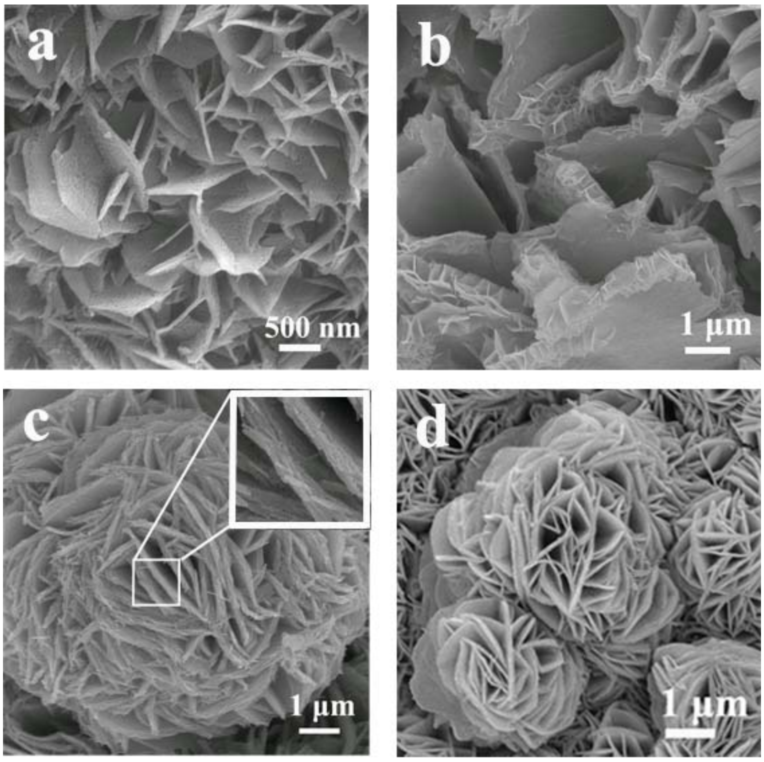

Fig. S3 SEM images of NiMnFe-IWM-C prepared with different precursor concentrations: (a) 0.10 mol/L Ni^{2+} and 0.10 mol/L Mn^{2+}, (b) 0.15 mol/L Ni^{2+} and 0.15 mol/L Mn^{2+}, (c) 0.25 mol/L Ni^{2+} and 0.25 mol/L Mn^{2+} and (d) 0.28 mol/L Ni^{2+} and 0.28 mol/L Mn^{2+}.

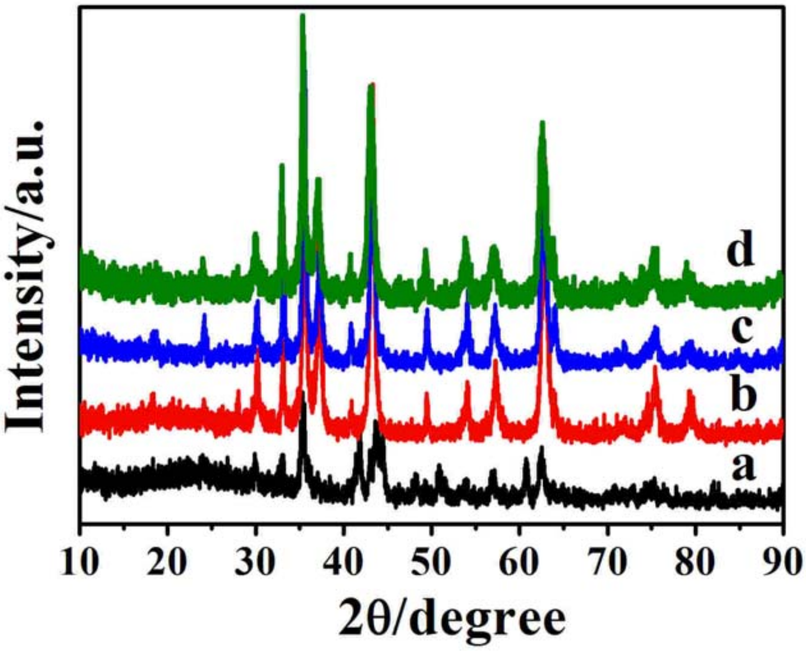

Fig. S4 XRD patterns of NiMnFe-IWM-C prepared with different precursor concentrations: (a) 0.10 mol/L Ni^{2+} and 0.10 mol/L Mn^{2+}, (b) 0.15 mol/L Ni^{2+} and 0.15 mol/L Mn^{2+}, (c) 0.25 mol/L Ni^{2+} and 0.25 mol/L Mn^{2+} and (d) 0.28 mol/L Ni^{2+} and 0.28 mol/L Mn^{2+}. The powders are scraped from the iron wire meshes.

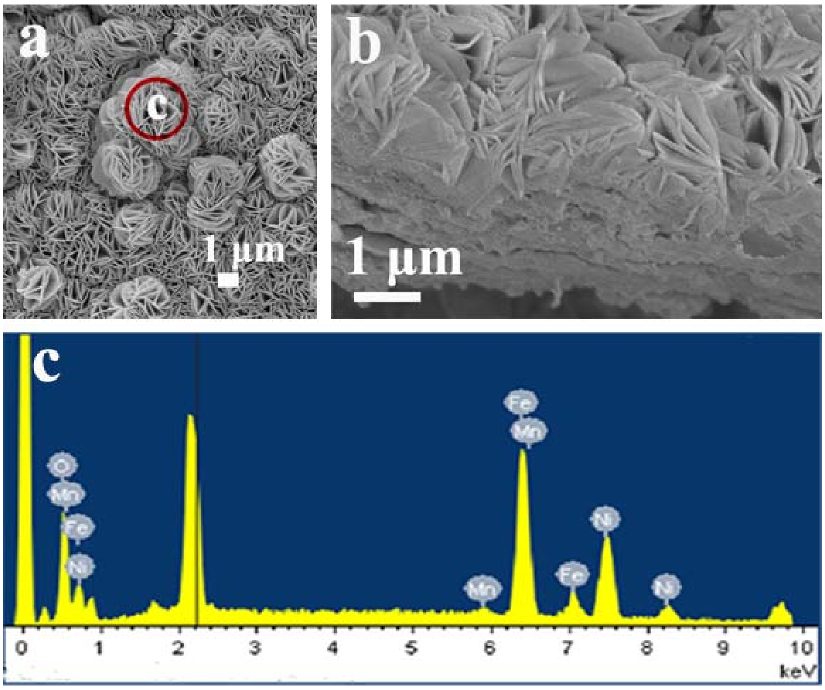

Fig. S5 SEM images of (a) surface morphology and (b) cross-sectional microstructure of NiMnFe-IWM-C. The EDX spectrum of the position in the surface morphology is shown in (c).

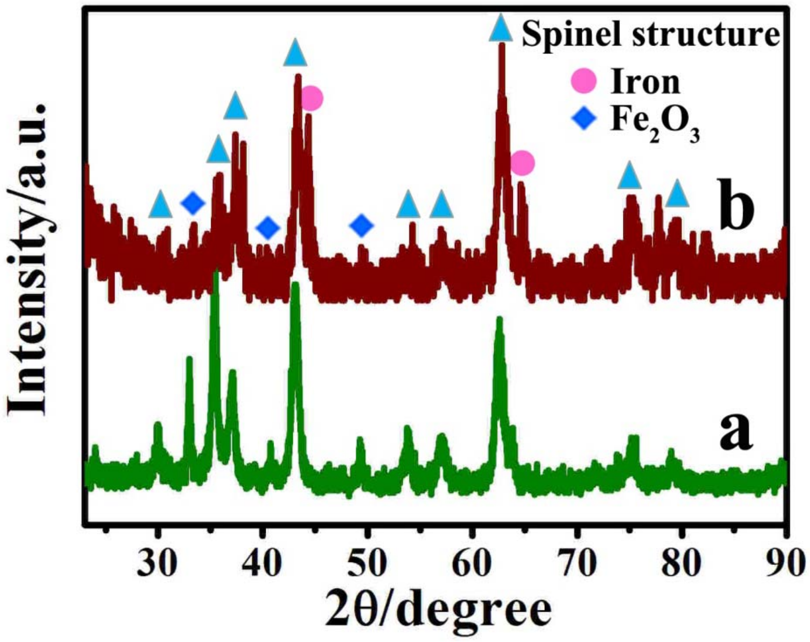

Fig. S6 XRD patterns of NiMnFe-IWM-C: (a) the powders scraped from the iron wire meshes and (b) the monolithic catalyst.

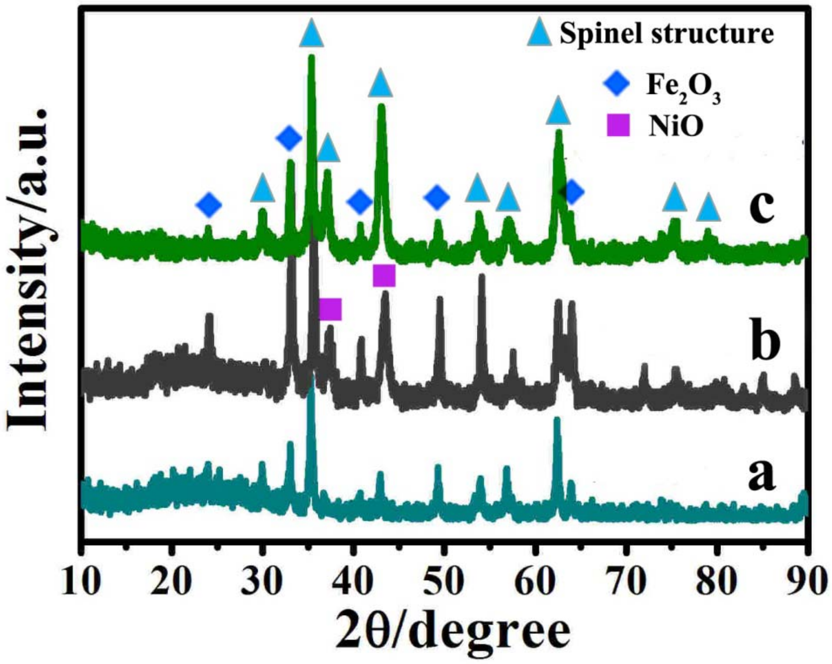

Fig. S7 XRD patterns of the products prepared by different methods: (a) FeFe-IWM-C, (b) NiMn-FeFe by impregnation*, (c) NiMnFe-IWM-C. The powders are scraped from the iron wire meshes.

* The powder is prepared by mixing $Ni(NO_3)_2$, $Mn(NO_3)_2$ and FeFe-IWM-C scraped from substrate at room temperature for 12h (according to the result of ICP-AES) , and then it is dried at 100 °C for 5 h. Finally calcined in air at 500 °C for 5 h.

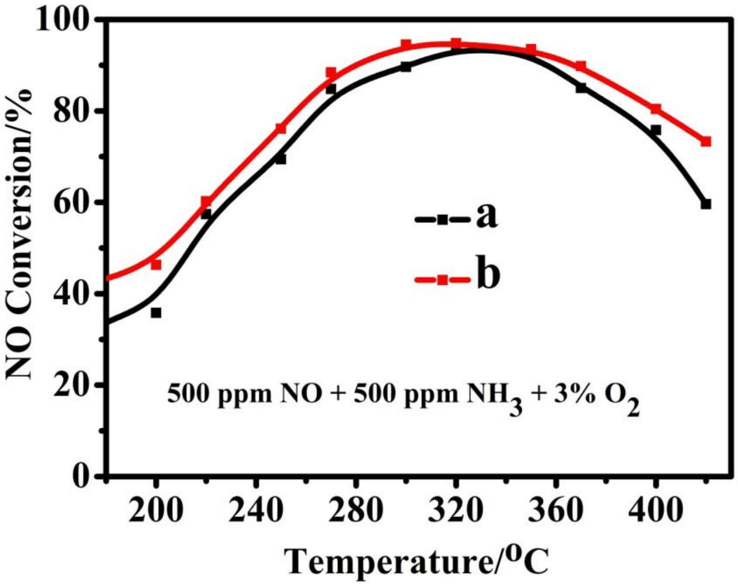

Fig. S8 NO conversions of NiMnFe-IWM-C under gas hourly space velocity of 20000 h^{-1}: (a) the monolithic catalyst and (b) the powders scraped from the iron wire meshes.

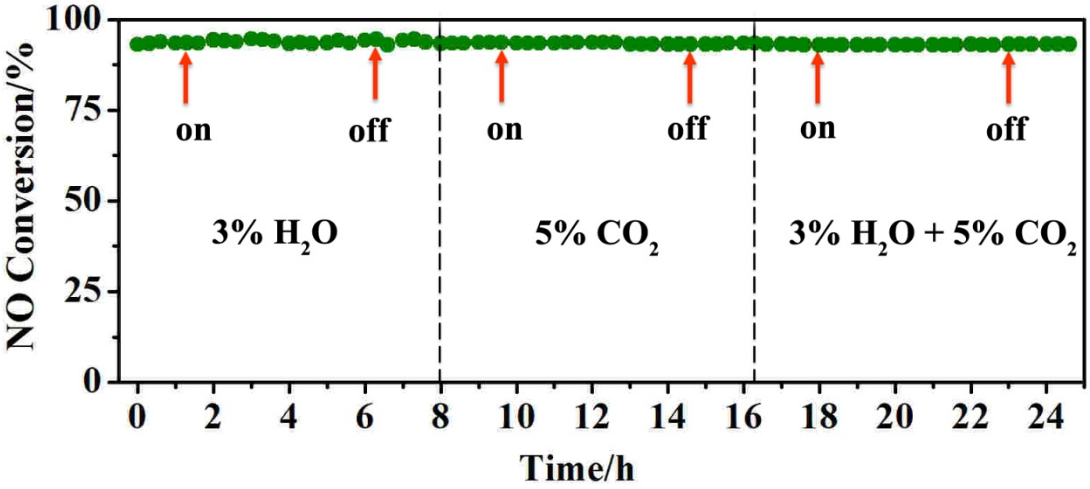

Fig. S9 Effect of H_2O and/or CO_2 on NO conversion over NiMnFe-IWM-C at 350 °C. Reaction conditions: [NO] = [NH_3] = 500 ppm, [O_2] = 3 vol.%, [H_2O] = 3 vol.%, [CO_2] = 5 vol.%, N_2 balance and GHSV = 20000 h^{-1}.

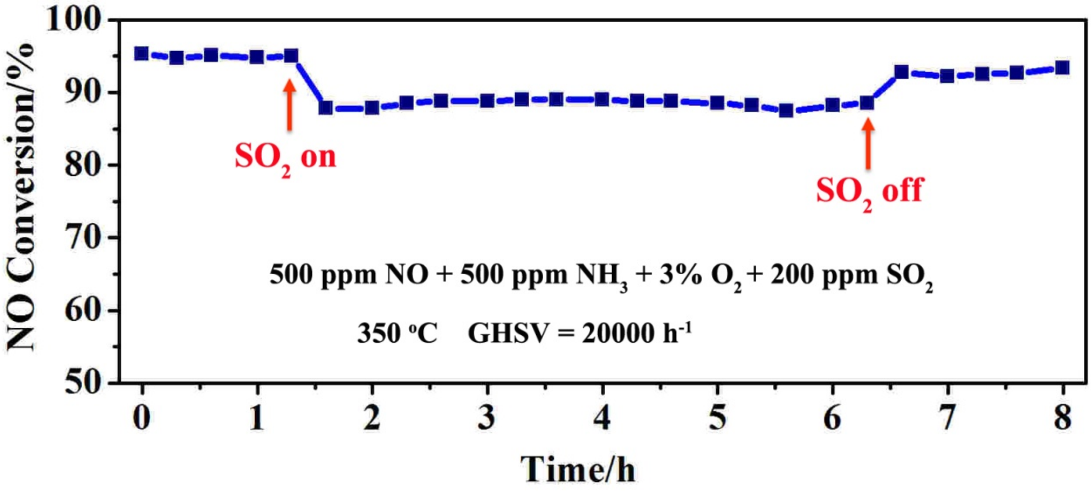

Fig. S10 Effect of SO_2 on NO conversion over NiMnFe-IWM-C at 350 °C. Reaction conditions: [NO] = [NH_3] = 500 ppm, [O_2] = 3 vol.%, [SO_2] = 200 ppm, N_2 balance and GHSV = 20000 h^{-1}.

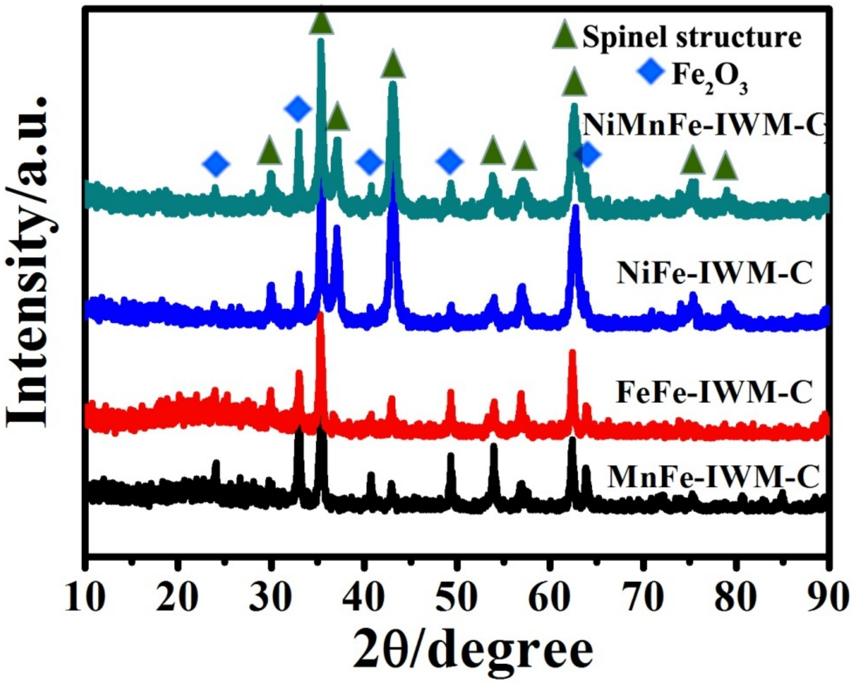

Fig. S11 XRD patterns of monolith catalysts. The powders are scraped from the iron wire meshes.

Table S1 Ni, Mn and Fe contents of the NiMnFe-IWM-C scraped from the iron wire meshes by ICP-AES analysis

sample	Composition (wt.%) Ni	Mn	Fe	(Ni+Mn)/Fe (atomic ratio)
	15.3	0.3	50.8	0.3

Table S2 EDX results of NiMnFe-IWM-C

Element*	Weight /%	Atomic /%
O K	7.42	22.25
Mn K	1.43	1.25
Fe K	47.68	40.97
Ni K	43.47	35.53

* The atomic ratio of (Ni+Mn)/Fe is calculated to be 0.90.

Table S3 Atom percentage of NiMnFe-IWM-C determined by XPS, binding energies and the percent of differential valence state.

XPS spectra*	Atomic /%	Element Valence	Binding energies	Percent of valence state /%
Ni 2p /eV	10.0	Ni^{2+}	854.7	58.2
		Ni^{3+}	861.4	41.8
Mn 2p /eV	0.4	Mn^{2+}	640.6	1.0
		Mn^{3+}	642.0	24.6
		Mn^{4+}	644.3	74.4
Fe 2p /eV	11.0	Fe^{2+}	710.9	38.5
		Fe^{3+}	712.2	61.5

* The atomic ratios of (Ni + Mn)/Fe and (Ni + Mn + Fe^{2+})/Fe^{3+} are calculated to be 0.94 and 2.16, respectively.

Part III. Additional discussion

Affecting factors and possible formation mechanism

In order to gain insight into the formation mechanism of the flower-like structure, a series of controlled experiments with different reaction time and different precursor concentrations were performed. The morphology and phase of products were studied by SEM and XRD measurements.

The effect of varying the reaction time on the microstructure of the film was investigated with a fixed Ni and Mn concentration of 0.28 mol/L, a fixed hydrothermal temperature of 150 °C, and variable reaction time of 2, 4, 10 and 12 h. The morphologies of the corresponding samples are compared as Fig. S1 depicts. After 2 h, the hexagonal nanosheets firstly grow from the iron wire (Fig. S1a), and the XRD pattern (Fig. S2) presents the characteristic of nanocrystalline of NiMnFe mixed metal oxides.[1, 2] The size of the nanosheets increase with reaction time. When proceeding for 4 h, the flower-like structure formed of curved sheet-like microcrystals starts to form at the current time (Fig. S1b). Some small particles that have not turned into the structure are still found on the surface. Increasing the reaction time to 10 h, the surface became rougher with the growth of flower-like structure (Fig. S1c). When the reaction was kept for 12 h (Fig. S1d), more homogeneous well-defined flower-like structures with smooth nanosheets were prepared due to the Ostwald ripening.[3, 4] Therefore, the in situ crystallization technique involves direct growth of NiMnFe-LDH crystallites on an iron substrate not with parallel face-to-face stacking of platelets, which can be explained by a heterogeneous nucleation mechanism including re-crystallization of primary building units.[5, 6] The XRD pattern of the samples show the same peaks over the whole reaction time (Fig. S2).

The precursor concentration was also varied. The films were prepared with a fixed hydrothermal temperature of 150 °C, a fixed reaction time of 12 h, and variable Ni and Mn concentrations of 0.10, 0.15, 0.25 and 0.28 mol/L. From Fig. S3, we could find that the concentration of Ni and Mn plays a key role on the growth of the flower-like structure. In Fig. S3a, the hexagonal nanosheet LDH crystals vertically grow on the substrate.[1, 7,

[8] The film clearly becomes more compact with increasing metal ion concentrations and each platelet was growing higher and wider (Fig. S3b). Some small nanosheets are formed on the end of the hexagonal nanosheet LDH crystals and grow into the flower-like structure (Fig. S3c and S3d). The XRD pattern of the products show almost the same peaks except that of Ni and Mn concentration of 0.10 mol/L (Fig. S4), in which the peaks of FeO were observed due to incomplete reactions.

On the basis of the investigation and analysis above, the possible formation mechanism of the flower-like structure was proposed. Firstly, the iron substrate was partially dissolved by OH^- produced from NH_4OH and NH_4Cl hydrolysis, which acted as a crucial step initiating the construction of the flower-like structure.[9, 10] The iron wire mesh used in this study also contributes to the component of final products. Amorphous $Fe(OH)_3$ is first formed. An addition of sodium citrate makes the pH deposition range of $Fe(OH)_3$ in the solution raise because Fe^{3+} ions are chelated by sodium citrate.[11, 12] Meanwhile, the added sodium citrate mainly exists as $C_6H_5O_7^{3-}$ ions because of the OH^- ions liberated by the NH_4Cl hydrolysis. $C_6H_5O_7^{3-}$ ions induce Fe^{3+} ions in the solution to form the metal–ligand $[Fe(C_6H_4O_7)_2]^{5-}$.[13] Usually, Ni^{2+} and Mn^{2+} ions are transported from the solution to the surface of the substrate (Fig. 1a), and then the slow hydrolysis of NH_4Cl keeps the pH value of the reaction medium, suitable for the growth of LDH crystallites on the substrate. At this condition, the direct conversion of $Fe(OH)_3$ to NiMnFe-LDH is probably replaced by the following reactions.

$$Fe^{3+} + 3OH^{-} \rightarrow Fe(OH)_3 \tag{1}$$

$$Fe(OH)_3 + 2C_6H_5O_7^{3-} \leftrightarrow [Fe(C_6H_4O_7)_2]^{5-} + OH^{-} + 2H_2O \tag{2}$$

$$x[Fe(C_6H_4O_7)_2]^{5-} + yNi^{2+} + zMn^{2+} + CO_3^{2-} + OH^{-} + nH_2O \rightarrow [Ni_yMn_zFe_x(OH)_{2y+2z+3x}]$$
$$(CO_3^{2-}) \cdot nH_2O + 2x\ C_6H_5O_7^{3-} \tag{3}$$

$$[Ni_yMn_zFe_x(OH)_{2y+2z+3x}]\ (CO_3^{2-}) \cdot nH_2O \rightarrow Ni_yMn_zFe_xO_{y+z+3/2x} + CO_2 + nH_2O \tag{4}$$

Following the aggregation of nanoparticles into nanosheets, relatively small thin slices grew slowly on the surface of nanosheets (Fig. S3b), because the NiMnFe-LDH will preferentially adsorb and bond to the active sites of nanosheets, which is similar to the previous reports.[6, 14, 15] Finally, the flower-like structure formed through oriented growth of nanosheets at the expense of adjacent smaller nanoparticles which can be referred to the Ostwald ripening process.[4, 16, 17] Specifically, the NiMnFe-LDH continuously attaches and bonds to the surface of larger flakes in order to achieve a minimum total free energy.[2, 18-22]

Elemental analysis

The elemental information of catalysts was investigated by means of ICP-AES (Table S1), EDX (Table S2) and XPS (Table S3). It is found that the atomic ratio of (Ni+Mn)/Fe calculated by EDX is consistent with that by XPS. Because the inner Fe from the iron wire mesh can be detected by ICP-AES, the atomic ratio of (Ni+Mn)/Fe determined by ICP-AES is lower than that by EDX or XPS.

The XPS spectra of Ni2p, Mn2p and Fe2p are shown in Fig. 3b-d. As shown in Fig. 3b, in the Fe 2p range of monolith catalysts, the Fe $2p_{3/2}$

peaks are narrower and stronger than those of Fe $2p_{1/2}$ because of the spin-orbit (j–j) coupling, which can be decomposed into a doublet and two broad asymmetric satellites while Fe $2p_{1/2}$ has only two in the spinel structure. The Fe $2p_{3/2}$ doublet is at ~710 eV and the second at ~712 eV.[23] The presence of Fe^{2+} and Fe^{3+} is confirmed by the charge transfer satellite of Fe $2p_{3/2}$ at ~ 714 eV and ~729 eV and by the value of the Fe $2p_{3/2}$–Fe $2p_{1/2}$ splitting of ~ 13.6 eV.[24] It is clearly seen from Fig. 3b that the surface iron species of the catalysts mainly exists in the form of Fe^{3+} together with minor Fe^{2+}.[25] The main redox reaction of NO on the surface occurrs on Fe^{3+},[26] the proportion of which in the NiMnFe-IWM-C is higher than other catalysts. In Fig. 3c, the high–resolution Ni2p spectrum displayed two peaks including $Ni2p_{3/2}$ and $Ni2p_{1/2}$ at 851–859 eV and 869–876 eV, which indicates the presence of ionic nickel species. Thus, Ni was present in +2 and +3 valence states in the catalyst with ions residing in octahedral sites of a spinel-like structure. Meanwhile the observation of satellite, which is the fingerprint of Ni^{2+}, can be taken as the proof of the presence of an important percent of Ni^{2+} on the catalyst surface.[27] However, it was observed that Ni was mainly present in +2 valence states and few +3 valence states. It implied that redox reaction occurred on the surface and Ni^{2+} provided the electrons, indicating the involvement of $Ni^{2+} \leftrightarrow Ni^{3+} \leftrightarrow Ni^{2+}$ redox processes during the reaction. As Mn cation was introduced into the system, Mn^{2+} (640.6 eV), Mn^{3+}

(642.0 eV) and Mn^{4+} (644.3 eV) appear on MnFe-IWM-C and NiMnFe-IWM-C (Fig. 3d). The percent of Mn^{4+} cation on NiMnFe-IWM-C obviously increases as compared with that on MnFe-IWM-C. [28]

REFERENCES

1. Z. Lü, F. Zhang, X. Lei, L. Yang, D. G. Evans and X. Duan, *Chem Eng Sci*, 2007, **62**, 6069-6075.
2. X. Li, J. Liu, X. Ji, J. Jiang, R. Ding, Y. Hu, A. Hu and X. Huang, *Sensor Actuat B-Chem*, 2010, **147**, 241-247.
3. X. Xiang, G. Fan, J. Fan and F. Li, *J Alloy Compd*, 2010, **499**, 30-34.
4. J. Kong, W. Liu, F. Wang, X. Wang, L. Luan, J. Liu, Y. Wang, Z. Zhang, M. Itoh and K.-i. Machida, *J Solid State Chem*, 2011, **184**, 2994-3001.
5. S. He, Y. Zhao, M. Wei, D. G. Evans and X. Duan, *Ind Eng Chem Res*, 2012, **51**, 285-291.
6. X. Guo, S. Xu, L. Zhao, W. Lu, F. Zhang, D. G. Evans and X. Duan, *Langmuir*, 2009, **25**, 9894-9897.
7. X. Guo, F. Zhang, S. Xu, Z. Cui, D. G. Evans and X. Duan, *Ind Eng Chem Res*, 2009, **48**, 10864-10869.
8. H. Chen, F. Zhang, S. Xu, D. G. Evans and X. Duan, *Ind Eng Chem Res*, 2008, **47**, 6607-6611.
9. H. Chen, F. Zhang, S. Fu and X. Duan, *Adv Mater*, 2006, **18**, 3089-3093.
10. J.-K. Lin, J.-Y. Uan, C.-P. Wu and H.-H. Huang, *J Mater Chem*, 2011, **21**, 5011-5020.
11. Y. F. Han, H. J. Li, X. R. Ma and Z. H. Liu, *Solid State Sci*, 2009, **11**, 2149-2155.
12. Y. F. Han, Z. H. Liu, Z. P. Yang, Z. L. Wang, X. H. Tang, T. Wang, L. H. Fan and K. Ooi, *Chem Mater*, 2008, **20**, 360-363.
13. M. Matzapetakis, C. P. Raptopoulou, A. Tsohos, V. Papaefthymiou, N. Moon and A. Salifoglou, *J Am Chem Soc*, 1998, **120**, 13266-13267.
14. H. Wang, C. Zheng and F. Li, *Chem Eng J*, 2010, **158**, 633-640.
15. V. Prevot, N. Caperaa, C. Taviot-Gueho and C. Forano, *Cryst Growth Des*, 2009, **9**, 3646-3654.
16. T. Xiao, Y. Tang, Z. Jia, D. Li, X. Hu, B. Li and L. Luo, *Nanotechnology*, 2009, **20**, 475603.
17. B. Li and J. He, *J Phys Chem C*, 2008, **112**, 10909-10917.
18. X. Guo, F. Zhang, S. Xu, D. G. Evans and X. Duan, *Chem Commun*, 2009, 6836-6838.
19. M. S. Yang, J. F. Liu, Z. Chang, G. R. Williams, D. O'Hare, X. H. Zheng, X. M. Sun and X. Duan, *J Mater Chem*, 2011, **21**, 14741-14746.
20. L. Sun and C. Hu, *Mater Res Bull*, 2011, **46**, 1922-1927.
21. H. Wang, G. L. Fan, C. Zheng, X. Xiang and F. Li, *Ind Eng Chem Res*, 2010, **49**, 2759-2767.
22. M. D. Martinez-Ortiz, E. Lima, V. Lara and J. M. Vivar, *Langmuir*, 2008, **24**, 8904-8911.
23. M. V. Bukhtiyarova, A. S. Ivanova, E. M. Slavinskaya, L. M. Plyasova, V. V. Kaichev and P. A. Kuznetsov, *Appl Catal A-Gen*, 2010, **384**, 230-240.
24. J. Janas, J. Gurgul, R. P. Socha, T. Shishido, M. Che and S. Dzwigaj, *Appl Catal B-Environ*, 2009, **91**, 113-122.

25. R. D. Zhang, D. J. Shi, Y. L. Zhao, B. H. Chen, J. Xue, X. Liang and Z. G. Lei, *Catal Today*, 2011, **175**, 26-33.
26. B. X. Shen, T. Liu, N. Zhao, X. Y. Yang and L. D. Deng, *J Environ Sci-China*, 2010, **22**, 1447-1454.
27. Z. Ma, X. Gao, X. Yuan, L. Zhang, Y. Zhu and Z. Li, *Catal Commun*, 2011, **12**, 817-821.
28. S. J. Yang, C. Z. Wang, J. H. Li, N. Q. Yan, L. Ma and H. Z. Chang, *Appl Catal B-Environ*, 2011, **110**, 71-80.